ORIGINAL

Ines Gilch [ID] · **Tobias Neuwirth** [ID] · **Benedikt Schauerte** ·
Nora Leuning · **Simon Sebold** [ID] · **Kay Hameyer** ·
Michael Schulz · **Wolfram Volk**

Impact of residual stress evoked by pyramidal embossing on the magnetic material properties of non-oriented electrical steel

Abstract Targeted magnetic flux guidance in the rotor cross section of rotational electrical machines is crucial for the machine's efficiency. Cutouts in the electrical steel sheets are integrated in the rotor sheets for magnetic flux guidance. These cutouts create thin structures in the rotor sheets which limit the maximum achievable rotational speed under centrifugal forces and the maximum energy density of the rotating electrical machine. In this paper, embossing-induced residual stress, employing the magneto-mechanical Villari effect, is studied as an innovative and alternative flux barrier design with negligible mechanical material deterioration. The overall objective is to replace cutouts by embossings, increasing the mechanical strength of the rotor. The identification of suitable embossing geometries, distributions and methodologies for the local introduction of residual stress is a major challenge. This paper examines finely distributed pyramidal embossings and their effect on the magnetic material behavior. The study is based on simulation and measurements of specimen with a single line of twenty embossing points performed with different punch forces. The magnetic material behavior is analyzed using neutron grating interferometry and a single sheet tester. Numerical examinations using finite element analysis and microhardness measurements provide a more detailed understanding of the interaction of residual stress distribution and magnetic material properties. The results reveal that residual stress induced by embossing affects magnetic material properties. Process parameters can be applied to adjust the magnetic material deterioration and the effect of magnetic flux guidance.

Keywords Residual stress · Magneto-mechanical coupling · Neutron grating interferometry · Magnetic flux barrier · Embossing

1 Introduction

The development toward electromobility and the connected demand for energy-efficient electrical machines requires further progress and alternatives in the processing and construction of rotating electrical machines. Especially permanent magnet synchronous machines (PMSM) [1] and synchronous reluctance machines (SynRM) [2] are gaining significance in this field. Both electrical machine topologies require an optimal

I. Gilch (✉) · W. Volk
Chair of Metal Forming and Casting (utg), Walther-Meißner-Str. 4, 85748 Garching, Germany
E-mail: ines.gilch@utg.de

T. Neuwirth· S. Sebold · M. Schulz
Heinz Maier-Leibnitz Zentrum (MLZ), Lichtenbergstr. 1, 85748 Garching, Germany
E-mail: tobias.neuwirth@frm2.tum.de

B. Schauerte· N. Leuning · K. Hameyer
Institute of Electrical Machines (IEM), Schinkelstr. 4, 52070 Aachen, Germany
E-mail: benedikt.schauerte@iem.rwth-aachen.de
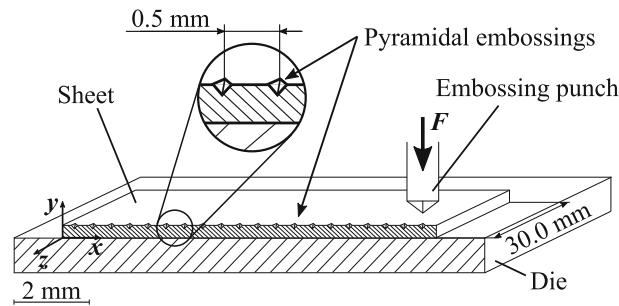
Fig. 1 Schematic illustration of the sequential embossing process with a flat die and pyramidal punch

magnetic flux guidance in the rotor with minimal stray flux and high angular velocity for improved energy efficiency [3].

Currently, cutouts in the rotor sheets are used for magnetic flux guidance and for stray flux suppression to increase the magnetic coupling between rotor and stator [4]. These cutouts reduce the mechanical strength of the rotor construction limiting the maximum angular velocity of electrical machines [5]. A novel approach for the design of magnetic flux barriers is embossing-induced mechanical stress to pin the magnetic domains using the *Villari*-effect, also known as inverse magnetostrictive effect. Pinned magnetic domains lead to decreased magnetic permeability in the mechanically modified material volume. These areas then act as magnetic flux barriers, suppressing the magnetic flux in undesired directions with negligible mechanical weakening of the rotor construction. Replacing cutouts partly or entirely by these alternative flux barriers can increase the mechanical strength of the rotor construction and enables higher angular velocities, resulting in an increase of the machine's power density. In previous works [6–9], we already demonstrated that embossing induced residual stress in non-oriented (NO) electrical steel can be used to guide magnetic flux. The embossing process in these examinations results in strong plastic deformation of the specimen geometry. Rotors and stators of electrical machines are constructed by stacking multiple electrical steel sheets; hence, the deformed sheet must be stackable to reach the necessary packing density and the insulation on the sheet surface needs to be maintained. Consequently, this paper deals with the examination of finely distributed multiple small embossing points and hence a different residual stress distribution compared to the previous studies and their effect on the magnetic material behavior. After the embossing process, mechanical finite element simulations provide a detailed understanding of the residual stress distribution in the specimens. Microhardness tests in conjunction with local and global magnetic measurements validate the simulation results.

As embossing causes work hardening, the increase in microhardness was evaluated using a nanoindenter. The deteriorated magnetic permeability caused by embossing is globally evaluated using single sheet tests (SST). Similarly, the embossing induces a change in the magnetic domain distribution and mobility which was locally probed using neutron grating interferometry (nGI). Together these methods allow a detailed analysis of embossing-induced variations of magnetic material properties in the electrical steel specimen.

2 Methods

2.1 Specimen manufacturing process

For specimen fabrication, a fully processed NO electrical steel having a silicon content of 2.4 wt% and a sheet thickness of 0.35 mm was used. The yield strength of the material is 363 MPa, and the tensile strength is 464 MPa [10]. The contour of the specimen, 10 mm x 60 mm, is wire-cut to minimize the influence of processing on magnetic material properties of the electrical steel [11]. Due to its crystallographic texture, the NO electrical steel has slightly anisotropic material properties caused by the manufacturing process. Therefore, the long edge of all samples is aligned parallel to the rolling direction (RD). Specimen material, orientation and size are maintained from previous studies [6–8]. The embossed specimens were produced with a sequential embossing process illustrated in Fig. 1. The sketched coordinate system is used for all following figures, direction and plane descriptions. A four-sided pyramidal geometry with a tip angle of 136.5° and a flat die were used as embossing tools.

Twenty embossing points (EPs) per sample were fabricated in a line perpendicular to the RD centered on the specimen geometry. The EPs have a distance of 0.5 mm to the next neighbor and 0.25 mm to the edge of the

sheet. EP_1 is located at $x = 0.25$ mm and EP_{20} at $x = 9.75$ mm. The embossing experiments were conducted with an universal testing machine. A load cell with a nominal force of 500 N measures the embossing force, which varies between 50 N, 100 N, 200 N and 400 N. The specimen label is combined by the punch geometry, "Py" for pyramidal punch, and the embossing force, e.g., "100 N" for a punch force of 100 N.

2.2 Mechanical finite element analysis

Finite element analysis (FEA) is used to calculate the residual stress induced by embossing with a punch force of 100 N and 200 N. Based on the resulting residual stress distributions, these two different embossing strategies are compared. The embossing with sequential forming processes requires a three dimensional approach. It is sufficient to simulate half of the sample geometry, due to the punch's symmetry as well as the position of the embossing points and material properties. The symmetry boundary condition is selected with respect to the line of embossed points. The simulation is divided in two parts. First, twenty points are embossed sequentially with the pyramidal punch. Secondly, all external forces on the sheet are eliminated for the springback analysis to evaluate the resulting residual stress state. During embossing, the sheet surface touching the flat die is fixed in y-direction (Fig. 1). The symmetry is defined in the x-y-plane. For springback, the symmetry boundary condition is maintained and all tool parts are removed. The embossing simulation is performed with an explicit solver, the springback simulation with an implicit solver.

Punch and die are assumed to be rigid bodies, as their deformation compared to the sheet material is negligible. The sheet is discretized with 433500 linear hex-elements. Unphysical surface deformations were reduced by using enhanced hourglass-control. The element edge length varies between 0.01 mm and 0.35 mm. The material model of the electrical steel is based on the measured mechanical properties in [10]. The mechanical properties of NO electrical steel are almost homogeneous but vary slightly for different RD. Hence, an anisotropic material model based on a Hill'48 yield criterion was used for the calculation. The RD is parallel to the magnetic field and perpendicular to the symmetry plane.

After the springback analysis, the residual stress distribution is analyzed. Using a grid on the sheet surface, the stress is evaluated along paths vertical to the sheet surface. For each path of the grid, 65 to 84 values are gathered with a distance of 5 μm in y-direction. The paths are spaced apart by 0.1 mm in x- and z-direction. The average residual stress in the sheet plane is the mean hydrostatic stress $\sigma_{\text{Hydrostat}}$ for each path. The work by Naumoski et al. [12] points out that compressive stress has higher deteriorating effects on the magnetic material behavior than tensile stress. Hence, the residual stress distribution in the symmetry plane is analyzed separately for compressive and tensile stress values. For this evaluation, the maximum absolute principal stress $\sigma_{\text{Max. Principal (Abs)}}$ multiplied by the algebraic sign is selected. Additionally, the ratio of compressive to tensile residual stress values is evaluated for each path; thus, the number of compressive stress values divided by the total number of stress values per path. For the stress evaluation in the symmetry plane, a path distance of 0.01 mm was selected.

2.3 Experimental methods

2.3.1 Microhardness tests

The deformation of the electrical steel leads to changes in the microhardness of the material. Weiss et al. [10,13] analyzed the hardness changes of the material due to shear cutting. Close to the cutting edge, the microhardness increases in comparison to the unworked material.

For the microhardness tests, microsections of the embossed samples are prepared. The microsection divides the embossing structure along the symmetry plane, comparable to the simulation. The specimens are mounted in thermoplastic mounting compound, ground and polished with a minimum abrasive particle size of 1 μm.

To obtain a fine grid of hardness measurement points, the measurements are conducted with a hardness is measured using a *Berkovich* tip and a maximum load of 50 mN. The *Oliver-Pharr* method is applied for the microhardness evaluation [14]. The x- and y-distance of the measurement points is 20 μm, which is three times larger than the indent diameter. Due to long measurement time, the hardness tests are performed in the surrounding of one EP for each specimen. For each was selected to enhance the comparability. The results are compared to reference measurements of an unworked electrical steel sheet.
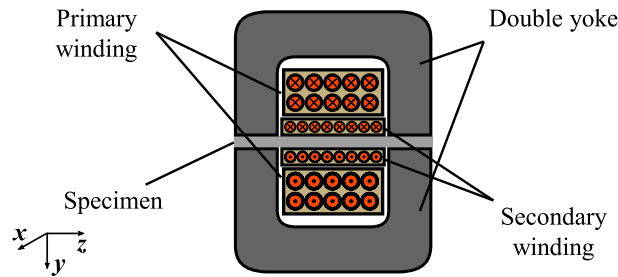
Fig. 2 Schematic illustration of the magnetically relevant parts of the SST setup

2.3.2 Neutron grating interferometry

The residual stress caused by embossing of electrical steel leads, due to the Villari effect, to a pinning of magnetic domains. This pinning effect results in a reduced response of magnetic domains to external magnetic fields [15] and effectively reduces the local magnetic permeability. Neutron grating interferometry (nGI) enables local analysis of bulk magnetic domain distribution.

nGI is a modern non-destructive neutron imaging technique based on Ultra-Small-Angle Neutron Scattering (USANS) [16]. Material or magnetic inhomogeneities in the micrometer range cause USANS, which is recorded spatially resolved using nGI. The underlying mechanism for the following examination is the interaction between the magnetic domains of electrical steel and the magnetic moment of the neutrons [17]. The resulting scattering map is called dark field image (DFI). Due to its construction, the nGI setup is tuned to be sensitive to specific structure sizes, i.e., the particular magnetic domain size. This size is called the correlation length of the nGI setup. In an applied magnetic field, a change in the magnetic domain size results in a changed scattering signal [7]. Hence, nGI enables the mapping of residual stress induced changes on the magnetic domains of electrical steel and therefore the local magnetic flux [6,18]. The nGI data presented in Sec. 3.2.2 has been acquired using the Talbot–Lau type nGI setup [7] of the ANTARES imaging beamline at FRM II [19,20]. The spatial resolution is 200 μm, while the correlation length of the interferometer was set to 0.84 μm. All data were normalized to an unworked electrical steel sheet.

2.3.3 Single sheet test measurements

While nGI allows to resolve the local magnetic domain distribution, a straightforward calculation of the magnetic permeability is not possible. Conversely, single sheet tests (SST) allow to analyze the global magnetic permeability of a specimen, but cannot analyze local effects. A sketch of a SST setup is depicted in Fig. 2. The specimen is placed within the primary and secondary winding, closing the magnetic core set up by the double yoke system. The excitation field of the primary winding is controlled in such a way that sinusoidal flux densities of defined excitation and frequency can be measured by the secondary winding. Typically, maximum magnetic flux densities are set from 0.1 to 1.8 T in 0.1 T steps. The magnetization frequency is 50 Hz. For the examination of embossed specimen, a SST setup with a yoke width of 60 mm is used.

To examine the correlation of mechanical stress and magnetic material properties an extended standard SST setup is used. The integrated load unit allows to directly evaluate the influence of globally applied unidirectional mechanical load on the magnetic material properties. A schematic overview of the measurement system is depicted in Fig. 3. The specimen size for these measurements was set to 100 mm x 600 mm. The yoke of the SST setup has a width of 120 mm. The acquired data can be used for the parametrization of a magnetization model considering the magneto-mechanical coupling for the FEA regarding the correlation of residual stress on the magnetic flux density.

In case of applied tensile load, the maximum strain of the specimen is limited by the yield strength of the electrical steel. Conversely, applying a compressive strain causes at low stress (< 10 MPa) a buckling of the specimen. As the embossing-induced stress decreases the permeability and acts as a flux barrier, an analysis of the global permeability with respect to the magnetic polarization allows to quantify the global effect of the flux barrier. In combination with nGI measurements, this enables the qualitative evaluation of the embossed flux barriers. By combining the results of the SST under load and the nGI measurements, the plausibility of the mechanical stress simulation can be verified.
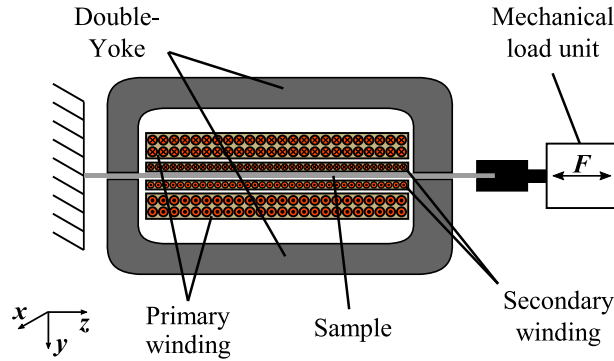
Fig. 3 Schematic illustration of the magnetically and mechanically relevant parts of the SST topology for magneto-mechanical measurements
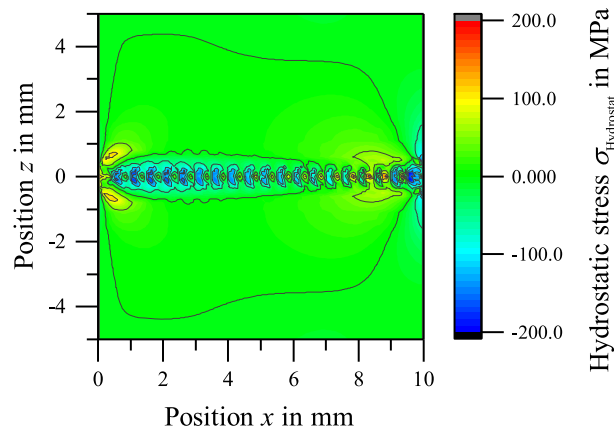
Fig. 4 Average hydrostatic stress component for pyramidal embossings with an embossing force of 100 N (Py100N). The stress component was calculated using paths perpendicular to the sheet surface

3 Results

3.1 Embossing-induced residual stress distribution (FEA)

The residual stress distribution across the sheet geometry is evaluated along paths perpendicular to the sheet surface. For each path the mean hydrostatic stress is computed. The stress distribution for Py100N is shown in Fig. 4. Close to the embossing points, -1.5 mm $< z < 1.5$ mm, the residual stress is increased compared to the unworked material ($\sigma \approx 0$ MPa). EP_2 to EP_{15} ($x = 0.75$ mm to 7.25 mm) as well as EP_{19} ($x = 9.25$ mm) and EP_{20} ($x = 9.75$ mm) are dominated by compressive stress. Tensile stress outweighs at EP_1 ($x = 0.25$ mm) and EP_{16} to EP_{18} ($x = 7.75$ mm to 8.75 mm). The results of the hydrostatic stress distribution in Py200N averaged over the sheet thickness are shown in Fig. 5. Compared to Py100N, the residual stress changes occur over a larger material volume -2.5mm $< z < 2.5$mm. The amount of tensile residual stress at EP_{11} to EP_{16} ($x = 5.25$ mm to 7.75 mm) is greater for Py200N than for Py100N. In total, the embossing produced with the higher load does show only a slight increase in residual stress maxima, but affects a larger material volume. This effect can be evaluated by calculating the standard deviation of the residual stress distribution over the full simulated volume. For Py100N, a standard deviation of 27.7 MPa was observed. This value rises to 36.2 MPa for Py200N.

The sequential embossing from $x = 0$ mm to 10 mm results in varying stress distributions for each embossing point. EP_1 (Py100N) or EP_1 and EP_2 (Py200N) are in average influenced by tensile hydrostatic stress. For Py100N embossing EP_2 to EP_{15} ($x = 0.75$ mm to 7.25 mm) as well as EP_{19} and EP_{20} show a dominance of compressive stress. For Py200N, this effect can be detected for EP_3 to EP_9 ($x = 1.25$ mm to 4.25 mm) and EP_{18} to EP_{20} ($x = 8.75$ mm to 9.75 mm). Especially the areas around EP_{16} to EP_{18} ($x = 7.75$ mm to 8.75 mm) (Py100N) and EP_{13} to EP_{17} ($x = 6.25$ mm to 8.25 mm) (Py200N) attract attention because of high tensile residual stress.
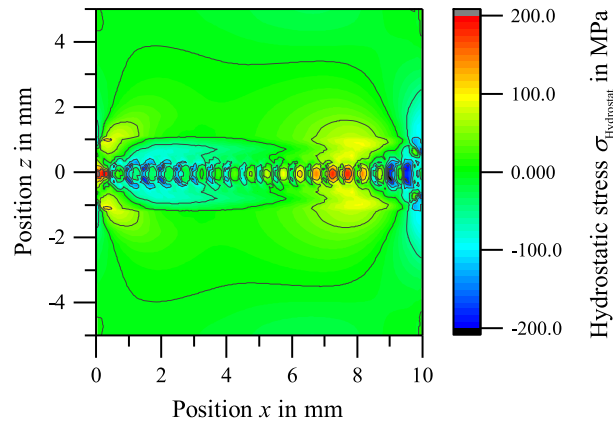
Fig. 5 Average hydrostatic stress component for pyramidal embossings with an embossing force of 200 N (Py200N). The stress component was calculated using paths perpendicular to the sheet surface
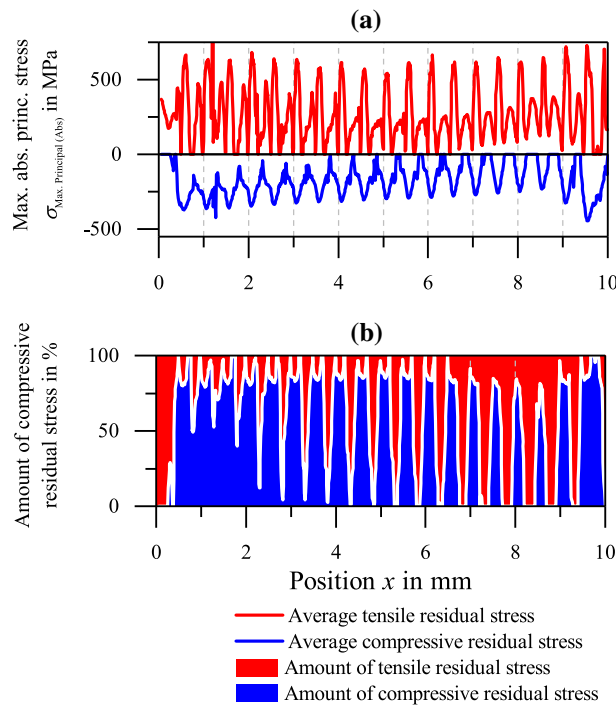
Fig. 6 Residual stress distribution along the x-axis averaged over the sheet thickness for Py100N: **a** distribution of maximum absolute principal stress split in tensile and compressive stress values; **b** relative amount of compressive residual stress values of the total number of stress values per path in the y-axis of the specimen

In Figs. 6a and 7a, the residual stress distribution along the x-axis averaged over the sheet thickness is plotted. The maximum absolute principal stress is split in tensile and compressive stress. Additionally, in Figs. 6b and 7b, the relative amount of compressive residual stress values to the total amount of stress values, evaluated along the paths in y-direction, is illustrated. For Py100N, the maxima of compressive stress are at 0.1 mm to 0.2 mm in positive x-direction next to the embossing points. The tensile residual stress shows maxima at almost the same x-positions as the compressive stress with additional maxima in between. The highest values observed for tensile and compressive residual stress are 696.8 MPa and -503.5 MPa, respectively.

In Fig. 6b, the relative amount of compressive residual stress values of the total number of stress values per path in $y-$direction of the specimen is shown. The amount of compressive residual stress is dominant between the embossing points. A higher amount of tensile residual stress values can be observed 0.1 μm to 0.15 μm before and after the embossing point. Generally, the relative amount of compressive residual stress values
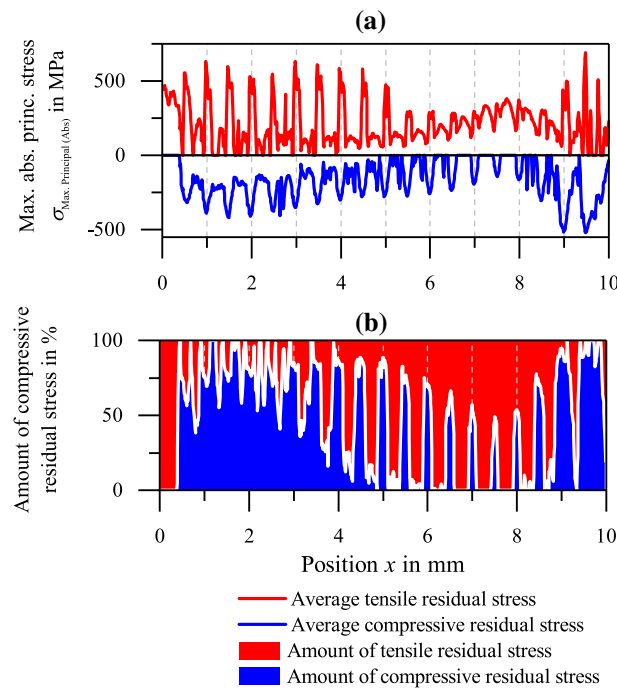
Fig. 7 Residual stress distribution along the x-axis averaged over the sheet thickness for Py200N: **a** distribution of maximum absolute principal stress split in tensile and compressive stress values; **b** relative amount of compressive residual stress values of the total number of stress values per path in the y-axis of the specimen

decreases from EP_1 ($x = 0.25$ mm) to EP_{18} ($x = 8.75$ mm). EP_{19} and EP_{20} show again a dominance of compressive residual stress over tensile stress.

The residual stress distribution of Py200N along the x-axis is depicted in Fig. 7. In general, the distribution of residual stress in Py200N in x-direction is not as homogeneous as for Py100N. The stress maxima are comparable to Py100N with 692.5 MPa and -518.8 MPa. For EP_1 to EP_{13} ($x < 6.25$ mm) Py200N shows tensile and compressive stress peaks between the EPs as seen for Py100N. The stress progression of EP_{14} to EP_{20} ($x > 6.75$ mm) is more irregular.

The amount of compressive residual stress values compared to the tensile values (Fig. 7b shows a similar but more distinct trend than Py100N. Between the embossing points, the amount of compressive residual stress has local maxima. For EP_2 to EP_7 ($x = 0.75$ mm to 3.25 mm), a dominance of compressive stress is evaluated which decreases continuously to $x = 7.75$ mm and increases again toward the edge of the sheet. The amount of tensile and compressive residual stress along the x-axis shows higher variance for Py200N than for Py100N. The compressive residual stress is concentrated on the first embossing points, whereas the tensile stress is more dominant on the section 5.5 mm $< x <$ 8.5 mm.

Generally, the residual stress distributions of both specimen show similarities, especially the maxima of tensile and compressive residual stress are at the same level. For Py200N, a larger material volume has an increased residual stress state and a more irregular distribution of tensile and compressive stress values. Furthermore, the sequential embossing leads to an irregular residual stress distribution and needs to be considered.

3.2 Experimental results

3.2.1 Microhardness

The nanoindentation measurements are used to determine the microhardness distribution in the microsection of one embossing point. As a reference, the hardness of unworked material was determined using 16 hardness indents. The mean hardness of the unworked electrical steel is 2.63 GPa. The hardness of the mounting material is 0.18 GPa in average.
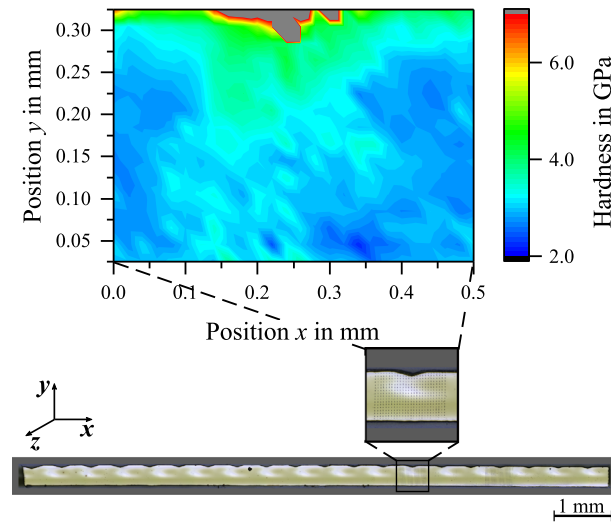
Fig. 8 Microhardness distribution in the vicinity of embossing point 14 of a pyramidal embossing with an embossing force of 100 N (Py100N)
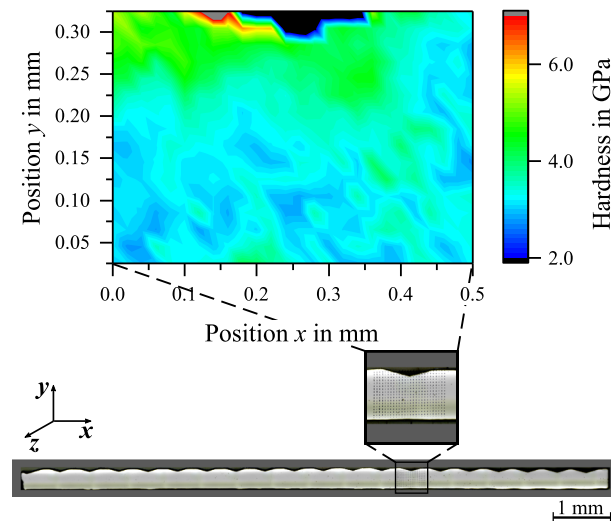
Fig. 9 Microhardness distribution in the vicinity of embossing point 14 of a pyramidal embossing with an embossing force of 200 N (Py200N)

Figures 8 and 9 illustrate the hardness distribution of the electrical steel sheet in the vicinity of one embossing point. Additionally, a microscope image of the intersection shows the embossings and the selected area for the microhardness tests. As the simulation indicates strong variations in residual stress distributions between different embossing points, the EP_{14} was chosen for both microhardness measurements. For Py100N, the increase in hardness is mainly focused to the area close to the embossing ($y > 0.2$ mm), see Fig. 8. Taking the geometry of the sheet into account, a few measurement points need to be rejected as they measure the junction between sheet and mounting material. The highest hardness measured, which can be assuredly allocated to the sheet, is 6.91 GPa. For 0 mm $< y <$ 0.15 mm the mean hardness is slightly increased with a value of 2.84 ± 0.16 GPa compared to the reference material.

In Fig. 9, an average increase of the hardness over the total sheet thickness can be observed for Py200N. The mean hardness for ($y = 0$ mm to 0.15 mm) is 3.11 ± 0.07 GPa, which is 18% higher than for the unworked reference. Close to the embossed surface, an additional rise of hardness is detected. The maximum value allocated to the sheet material is 6.91 GPa such as the maximum of Py100N. The hardness values smaller than 2 GPa are attributed to the mounting material.
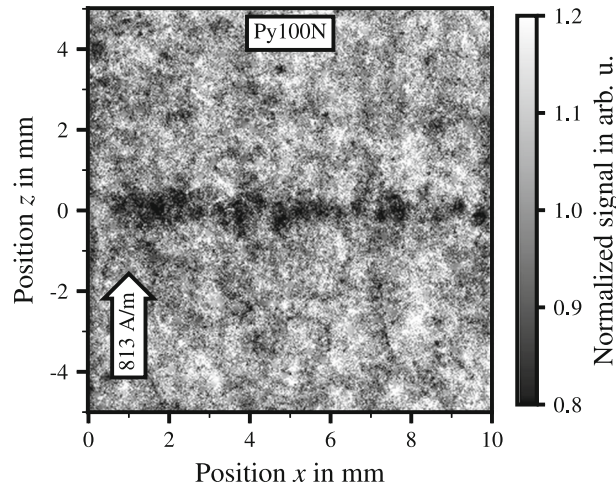
Fig. 10 Normalized nGI signal of Py100N. A magnetic field of 813 A/m has been applied in z-direction

In general, both embossed samples show work hardening whereas the total increase of hardness is higher for Py200N. The work hardening indicates the existence of grown residual stress. Using the microsections, the increase of sheet thickness in between the embossing points was evaluated. For Py100N, the sheet thickness increases in average by 1.5%. The sheet of Py200N has a final mean thickness of 367.8 µm, which is 105.1% of the original sheet thickness.

3.2.2 Magnetic domain distribution

With nGI, it is possible to track the pinning of the magnetic domains caused by the embossing induced residual stress. The pinning of the magnetic domains causes a change in magnetic permeability, altering the magnetic flux. By normalizing the DFI value of an embossed specimen to an unworked specimen, the embossing-induced scattering signal variation can be isolated. Hence, a signal above (below) unity typically denotes a higher (lower) amount of magnetic domains in the embossed specimen than in the unworked reference.

In Figs. 10 and 11, the respective normalized DFI value distribution of Py100N and Py200N as recorded by the nGI setup is presented. The applied external magnetic field strength H_A is 813 A/m. While the two different punch forces (100 N and 200 N) generate similar patterns, the signal strength obviously changes. Additionally, the size of the magnetically affected area increases concurrently with the embossing force. In Fig. 12, the average DFI signal trend in x-direction around the embossing line ($z = -0.5$ mm to 0.5 mm) for Py100N (black) and Py200N (red) is presented. The DFI signal of Py100N oscillates in between 0.85 and 1.07. A more distinct DFI signal progression is observed for Py200N. For $x = 0$ mm to 1.75 mm, the DFI signal drops from 1.05 to 0.70, followed by a rise to 0.95 at $x = 7.25$ mm. The curve is overlaid by a smeared oscillation with a period of the EP distance. At EP_{20} ($x = 9.75$ mm), the DFI signal shows again a local minimum of 0.73. The comparison of Py100N and Py200N in Fig. 12, shows only for $x = 6.75$ mm to 7.75 mm a lower DFI signal of Py100N. Hence, the reduction of magnetic flux compared to the unworked reference is higher for Py200N than for Py100N.

From previous works [21], as well as our own measurements on our specimen (Fig. 13), we know that compressive stress has a stronger influence on the magnetic permeability than tensile stress (Villari effect). Hence, we expect a reduced DFI signal in areas with compressive stress in contrast to areas with tensile stress or without stress. When comparing the DFI signal of Fig. 11 with the simulated stress map in Fig. 5, distinct patterns of the stress distribution can be recognized in the DFI signal. In areas of high compressive stress, such as the region from $x = 0.5$ mm to 3 mm and $z = -0.75$ mm to 0.75 mm or at the position $x = 9.75$ mm of the last embossing point EP_{20} from $z = -2.5$ mm to 2.5 mm, we observe a clear reduction of the DFI signal. In contrast, the DFI signal is less affected in areas of tensile stress. This can be seen for the first embossing point at $x = 0.25$ mm as well as for the larger area enclosed by $x = 6.5$ mm to 8.5 mm and $z = -1.5$ mm to 1.5 mm. This effect is similarly visible when comparing Fig. 7b with the red line in Fig. 12. In Py100N, a comparable correlation is visible, but less pronounced, see Figs. 4, 6b and 12.
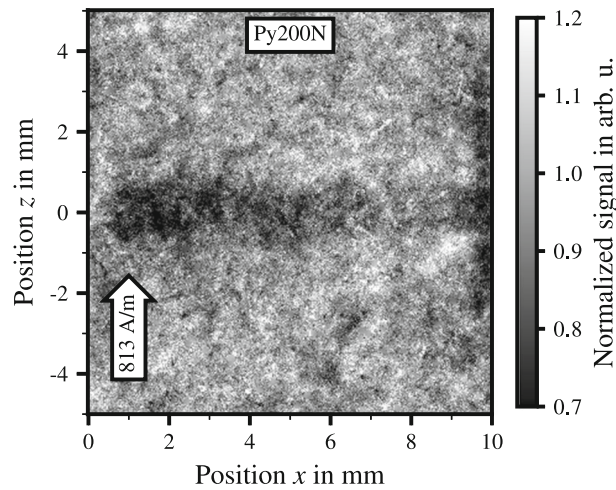
Fig. 11 Normalized nGI signal of Py200N. A magnetic field of 813 A/m has been applied in z-direction
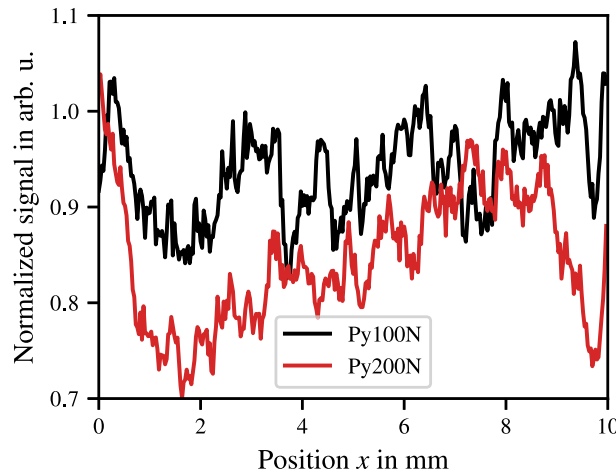
Fig. 12 Normalized nGI signal at the embossing line of Py100N (black) and Py200N (red). A magnetic field of 813 A/m has been applied in z-direction

3.2.3 Magnetizability

For the characterization of the magneto-mechanical coupling of the NO electrical steel sheets, SST measurements are performed using the mechanical loading SST setup. The comparison criterion is the relative magnetic permeability μ_r, which results from the quotient of the magnetic flux density and the magnetic field strength. A high value of relative permeability thus indicates a high magnetizability of the examined sample. The resulting permeability depending on the resulting mechanical stress and the magnetic excitation J_m are depicted in Fig. 13.

For tensile stress, the specimens are loaded to 413 MPa, exceeding yield strength. Concurrently with rising tensile stress, the relative permeability of the sample decreases continuously. With increasing mechanical load, the maximum permeability point moves toward lower magnetic polarizations. Nonetheless, regarding the permeability decrease, a certain saturation behavior can be observed. At a load of 51 MPa, the maximum permeability of the material is reduced by 47.8% when compared to the unworked reference material. A stress state of 103 MPa reduces the maximum permeability to 37.5%, 205 MPa results in 26.6% of initial permeability. For the plastically deformed NO electrical steel at a tensile stress of 413 MPa, the maximum permeability is about 18.0% of the maximum permeability of the unloaded sample.

In case of compressive load, a maximum stress value of -8.3MPa could be achieved without sheet buckling. Compared to the tensile stress state, the magnetic material properties react much more sensitively to the compressive load. A remarkable decrease in the magnetic permeability already occurs at -4.8MPa and
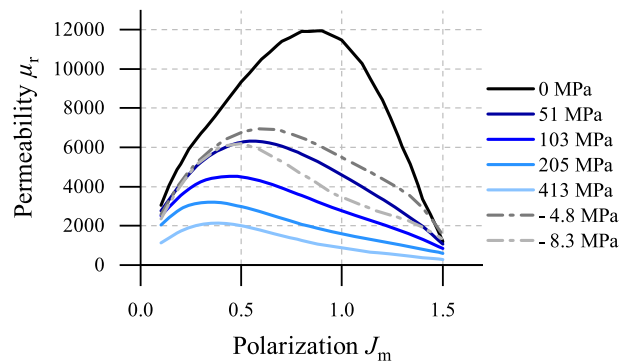
Fig. 13 Relative permeability with respect to polarization at tensile and compressive mechanical stress
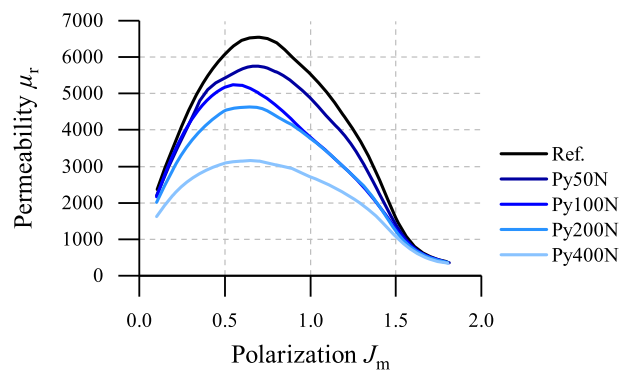
Fig. 14 Relative permeability with respect to polarization of embossed samples at increasing embossing forces

-8.3 MPa. This result is in agreement with other studies stating that compressive stress has a stronger influence on the magnetic behavior of non-oriented electrical steel sheets compared to tensile stress [22].

The measurements of the embossed specimens depicted in Fig. 14 show a behavior similar to the measurements under homogeneous applied mechanical load. As the embossing force increases, the magnetic permeability decreases as a result of the changed residual stress state. The permeability curve form depends on the embossing force and hence the resulting divergence in permeability between the specimen varies strongly with the applied polarization. The correlation between magnetic permeability and the duplication of embossing force shows no distinct pattern except of decreasing permeability. The simulated residual stress state of Py100N and Py200N results in similar maximum stress values but a higher embossing force leads to a greater area with increased residual stress and hence a rise in magnetic material deterioration. This leads to the conclusion that the affected material volume is crucial for the global magnetic material properties. When comparing Figs. 13 and 14, the measured permeability of the measurement performed at 0 MPa and the non-embossed reference specimen deviates in absolute values of the maximum permeability. The reason for this divergence is the varying sample geometry due to the use of different SST setups, resulting in a significantly stronger processing influence due to the higher ratio between sample volume and cut edge area of the embossed specimen. This leads to the consequence that the measurement results can only be compared qualitatively.

To sum up, the irregular distribution of tensile and compressive stress locally deteriorates the magnetic material properties which cannot be resolved with conventional magnetic measurement methods. Nonetheless, the globally averaged measurements of one single embossing line, within the much larger remaining unprocessed sample volume, already decreases the magnetic permeability by more than 50% for the case of an embossing force of 400 N.

4 Discussion

In this study, mechanical FEA, microhardness tests, SST and nGI measurements are utilized to analyze both the mechanical as well as magnetic properties of magnetic flux barriers produced by finely distributed embossing of

NO electrical steel. This wide-ranging analysis of embossed flux barriers connects the production of embossed electrical steel sheets, the analysis of the embossing influenced mechanical material properties and the effect of induced residual stress on the local and global magnetic material properties. For a detailed understanding of properties and functionality of embossing-induced residual stress as magnetic flux barriers, this profound examination is necessary. In previous studies, the theory of embossed magnetic flux barriers already could be proven [6–9]. To deepen the understanding of the interaction between residual stress and magnetic properties, further examination is necessary.

We performed this study to determine the relation between the embossing process, the induced residual stress distribution and the resulting magnetic material deterioration. As a result of the embossing sequence and the variation of embossing force, a distinct pattern is created in the residual stress map and hence the magnetic domain size distribution. Generally, the results prove that the effect of embossed flux barriers can be deliberately adjusted by the embossing force. Low embossing forces cause less plastic deformation of the electrical steel sheet and induce less residual stress compared to higher embossing forces. The mechanical simulation results of Py100N and Py200N show that the maximum tensile and compressive residual stress values are in the same order of magnitude and that the mechanical stress in the sheet plane is not confined to the embossing area. The distribution of the residual stress in the surrounding region increases with higher embossing forces. Furthermore, the influence of the embossing sequence on the residual stress distribution is remarkable.

Each embossing step leads to an elasto-plastic material deformation, which forms the embossing but causes a change in the residual stress state in nearby material volume, hence in the already embossed volume, too. The variation of process parameters, here the embossing force, affects in different ways the forming process and residual stress distribution. Maqbool and Bambach [23] observed a varying proportion of shearing, stretching and bending depending on the process parameters of a single point incremental forming process. An increase of the step down increment, hence the punch force and amount of deformation, rises the proportion of stretching and bending and reduces the amount of shearing. Maaß et al. [24] examined the residual stress state of parts formed with single point incremental forming under variation of the number of step down increments, which correlates with the punch force. The authors pointed out that these varied process parameters lead to a change in residual stress distribution. Hence, the influence of each forming step on the residual stress state of the surrounding material volume is strongly depending on the process parameters. We observed this effect for the two different embossing forces. Similarly, the free sheet edges at the first and last embossing point may not be neglected for the evaluated residual stress distribution. For the following discussion, the effect of the embossing sequence on the distribution of compressive and tensile residual stress is important, because compressive stress causes a stronger deterioration of the magnetic permeability, see chapter 3.2.3.

Embossing-induced plastic deformation causes work hardening and thus increases the hardness of the electrical steel. Additionally, the embossing-induced residual stress changes the magnetic domain size distribution which can be recorded using nGI. Hence, both microhardness analysis as well as nGI are used to validate the mechanical FEA. Py100N exhibits minor work hardening concentrated below the embossed surface ($y = 0.15$ mm to 0.35 mm), whereas the rest of the evaluated area shows barely any change in hardness. In contrast, Py200N reveals a distinctly increased microhardness over the whole sheet thickness, indicating higher residual stress in comparison to Py100N. For both measurements, the hardness distribution is not symmetrical to the central axis of the embossing, demonstrating the interaction of the sequential embossing points.

Evaluating the nGI data in Figs. 10 and 11 in the context of the numerical analysis in Figs. 4 and 5, a direct correlation of magnetic domain density and residual stress distribution exists. In regions with increased compressive stress, a lower DFI signal is detected, while areas with minor stress or tensile stress show comparatively higher DFI signals. The comparison of the normalized DFI signals of the two embossed specimens along the embossing line (Fig. 12) indicates an increased magnetic domain density and decreased magnetic flux at higher embossing forces. An exception is the area between $x = 6.75$ mm and $x = 7.75$ mm, where the DFI signal indicates a locally higher magnetic domain density in Py100N than in Py200N. This effect correlates with the locally higher residual stress maxima in Py100N when compared to Py200N in this area (see Figs. 6 and 7). The magnetic flux concentrates in the material volume with lower magnetic resistance which is the area with reduced compressive stress, increasing the evaluated DFI signal in this area. The nGI measurements qualitatively validate the numerical analysis.

Using the microscope images of the microsections, a local change in sheet thickness because of embossing is observed. As nGI measurements integrate over the specimens bulk volume, a variation in thickness results in a changed scattering signal, which has to be considered.

The results obtained by nGI measurements are supported by the SST measurements of electrical steel under homogeneous mechanical load, see Fig. 13 and [12]. Compressive stress in electrical steel causes stronger magnetic material deterioration, i.e., a substantially stronger decrease of permeability, compared to tensile stress. This characteristic of Villari effect explains the magnetic domain distribution caused by the inhomogeneous tensile and compressive residual stress distribution.

Finally, the global magnetic properties of the embossed specimen were examined. Additionally to Py100N and Py200N, samples embossed with punch forces of 50 N and 400 N have been measured using SST. As expected, samples embossed with higher forces show decreasing magnetic permeabilities. The rising amount of induced residual stress, which is spread over a larger material volume, increases the magnetic resistance. An one-to-one relationship between the measurements under homogeneously applied mechanical stress and the samples with different embossing forces cannot be carried out, due to the nonlinearity of the magneto-mechanical coupling and the inhomogeneous distribution of the residual stress in the sample volume.

5 Conclusion and outlook

In this study, we examined the influence of pyramidal embossings on the mechanical and magnetic material properties of electrical steel. Every sample was embossed sequentially with 20 embossing points, located in a line covering the full sample width, perpendicular to the applied magnetic field. The punch force was varied between 50 N and 400 N. Using FEA, we numerically simulated the embossing process (sequence and force) of the electrical steel specimen, generating a residual stress map. By analyzing the microhardness close to one embossing point, as well as using SST and nGI evaluating the global and local magnetic properties, we demonstrated the direct connection between the embossing process and the resulting magnetic permeability and the underlying magnetic domain distribution. We note that the embossing process strongly influences the tensile and compressive stress distribution which needs to be considered in future experiments. Tensile and compressive stress influenced the magnetic domain distribution with different magnitude, which we can map using nGI. The DFIs showed this effect locally, which cannot be detected by global measurements as carried out with the SST. The analyzed permeability of the whole specimen underlines the size of material volume affected by residual stress, which is as well examined by the standard deviation of hydrostatic stress values.

To gain further knowledge about the interaction of mechanical stress and magnetic material behavior, additional studies need to be carried out. Particularly, the measurement of residual stress distribution is necessary for a precise validation of the simulation results. For a more in-depth understanding, a magneto-mechanical simulation should be implemented. This allows to evaluate the magnetic flux distribution based on the numerically simulated residual stress distribution. Such a simulation may be validated by vector hysteresis measurements and nGI.

For the application of the embossed flux barriers in a rotating electrical machine, the effect of the embossing-induced residual stress for flux guidance has to be examined depending on the RD of the electrical steel. Furthermore, the residual stress state resulting from a simultaneous embossing of an electrical steel sheet needs to examined. This work shows the basics of innovative magnetic flux guidance with embossing-induced residual stress and proves that the effect of embossed magnetic flux barriers can be adjusted by process parameters.

Author contributions IG—conceptualization, specimen manufacturing, investigation (FEA, microhardness), writing original draft; TN—conceptualization, investigation (nGI measurements), writing original draft; BS—conceptualization, investigation (SST measurements), writing original draft; NL—investigation (SST measurements), writing: review and editing; SS—writing:

References

1. Juergens, J., Fricass, A., Marengo, L., Gragger, J., De Gennaro, M., Ponick, B.: Innovative design of an air cooled ferrite permanent magnet assisted synchronous reluctance machine for automotive traction application. In: 2016 XXII International Conference on Electrical Machines (ICEM), pp. 803–810 (2016)
2. Trancho, E., Ibarra, E., Arias, A., Kortabarria, I., Jurgens, J., Marengo, L., Fricass, A., Gragger, J.V.: PM-assisted synchronous reluctance machine flux weakening control for EV and HEV applications. IEEE Trans. Indus. Electron. **65**(4), 2986–2995 (2018)
3. Gerada, D., Mebarki, A., Brown, N.L., Gerada, C., Cavagnino, A., Boglietti, A.: High-speed electrical machines: Technologies, trends, and developments. IEEE Trans. Indus. Electron. **61**(6), 2946–2959 (2013)
4. Jung, J.W., Lee, B.H., Kim, D.J., Hong, J.P., Kim, J.Y., Jeon, S.M., Song, D.H.: Mechanical stress reduction of rotor core of interior permanent magnet synchronous motor. IEEE Trans. Magn. **48**(2), 911–914 (2012)
5. Chiodetto, N., Mecrow, B., Wrobel, R., Lisle, T.: Electro-mechanical challenges in the design of a high-speed-high-power-PMSM rotor for an aerospace application. In: 2019 IEEE Energy Conversion Congress and Exposition (ECCE), pp. 3944–3951 (2019)
6. Vogt, S., Neuwirth, T., Schauerte, B., Weiss, H.A., Falger, P.M., Gustschin, A., Schulz, M., Hameyer, K., Volk, W.: Extent of embossing-related residual stress on the magnetic properties evaluated using neutron grating interferometry and single sheet test. Prod. Eng. **13**(2), 211–217 (2019)
7. Neuwirth, T., Backs, A., Gustschin, A., Vogt, S., Pfeiffer, F., Böni, P., Schulz, M.: A high visibility talbot-lau neutron grating interferometer to investigate stress-induced magnetic degradation in electrical steel. Sci. Rep. **10**(1), 1–12 (2020)
8. Moll, I., Vogt, S., Neuwirth, T., Schauerte, B., Hameyer, K., Schulz, M., Gustschin, A., Volk, W., Weiss, H.A.: Analysis of cylindrically and spherically embossed flux barriers in non-oriented electrical steel. In: The 13th International Conference on the Technology of Plasticity. engrXiv (2020)
9. Schauerte, B., Leuning, N., Vogt, S., Moll, I., Weiss, H., Neuwirth, T., Schulz, M., Volk, W., Hameyer, K.: The influence of residual stress on flux-barriers of non-oriented electrical steel. J. Magn. Magn. Mater. p. 166659 (2020)
10. Weiss, H., Leuning, N., Steentjes, S., Hameyer, K., Andorfer, T., Jenner, S., Volk, W.: Influence of shear cutting parameters on the electromagnetic properties of non-oriented electrical steel sheets. J. Magn. Magn. Mater. **421**, 250–259 (2017)
11. Kurosaki, Y., Mogi, H., Fujii, H., Kubota, T., Shiozaki, M.: Importance of punching and workability in non-oriented electrical steel sheets. J. Magn. Magn. Mater. **320**(20), 2474–2480 (2008)
12. Naumoski, H., Riedmueller, B., Minkow, A., Herr, U.: Investigation of the influence of different cutting procedures on the global and local magnetic properties of non-oriented electrical steel. J. Magn. Magn. Mater. **392**, 126–133 (2015)
13. Weiss, H., Tröber, P., Golle, R., Steentjes, S., Leuning, N., Hameyer, K., Volk, W.: Loss reduction due to blanking parameter optimization for different non-grain oriented electrical steel grades. In: 2017 IEEE International Electric Machines and Drives Conference (IEMDC), pp. 1–7. IEEE (2017)
14. Oliver, W.C., Pharr, G.M.: Improved technique for determining hardness and elastic modulus using load and displacement sensing indentation experiments. J. Mater. Res. **7**(6), 1564–1580 (1992)
15. Moses, A., Ntatsis, A., Kochmann, T., Schneider, J.: Magnetostriction in non-oriented electrical steels: general trends. J. Magn. Magn. Mater. **215**, 669–672 (2000)
16. Pfeiffer, F., Grünzweig, C., Bunk, O., Frei, G., Lehmann, E., David, C.: Neutron phase imaging and tomography. Phys. Rev. Lett. **96**(21), 215505 (2006)
17. Grünzweig, C., David, C., Bunk, O., Dierolf, M., Frei, G., Kühne, G., Kohlbrecher, J., Schäfer, R., Lejcek, P., Rønnow, H., et al.: Neutron decoherence imaging for visualizing bulk magnetic domain structures. Phys. Rev. Lett. **101**(2), 025504 (2008)
18. Weiss, H., Steentjes, S., Tröber, P., Leuning, N., Neuwirth, T., Schulz, M., Hameyer, K., Golle, R., Volk, W.: Neutron grating interferometry investigation of punching-related local magnetic property deteriorations in electrical steels. J. Magn. Magn. Mater. **474**, 643–653 (2019)
19. Calzada, E., Gruenauer, F., Mühlbauer, M., Schillinger, B., Schulz, M.: New design for the ANTARES-II facility for neutron imaging at FRM II. Nuclear Instrum. Methods Phys. Res. Sect. A Accelerat. Spectrom. Detect. Associat. Equip. **605**(1–2), 50–53 (2009)
20. Schulz, M., Schillinger, B.: ANTARES: Cold neutron radiography and tomography facility. J. Large-Scale Res. Facilities JLSRF 1, 17 (2015)
21. Leuning, N., Steentjes, S., Hameyer, K., Schulte, M., Bleck, W.: Effect of material processing and imposed mechanical stress on the magnetic, mechanical, and microstructural properties of high-silicon electrical steel. Steel Res. Int. **87**(12), 1638–1647 (2016)
22. Miyagi, D., Miki, K., Nakano, M., Takahashi, N.: Influence of compressive stress on magnetic properties of laminated electrical steel sheets. IEEE Trans. Magn. **46**(2), 318–321 (2010)
23. Maqbool, F., Bambach, M.: Revealing the dominant forming mechanism of single point incremental forming (SPIF) by splitting plastic energy dissipation. In: 17th International Conference on Sheet Metal, pp. 188–193. SHEMET17 (2017)
24. Maaß, F., Hahn, M., Tekkaya, A.E.: Interaction of process parameters, forming mechanisms, and residual stresses in single point incremental forming. Metals **10**(5), 1–12 (2020)